The Astrophysical Journal, 729:19 (8pp), 2011 March 1 doi:10.1088/0004-637X/729/1/19

A DISTINCTIVE DISK–JET COUPLING IN THE SEYFERT-1 ACTIVE GALACTIC NUCLEUS NGC 4051

A. L. King[1], J. M. Miller[1], E. M. Cackett[2], A. C. Fabian[2], S. Markoff[3], M. A. Nowak[4], M. Rupen[5], K. Gültekin[1], and M. T. Reynolds[1]

[1] Department of Astronomy, University of Michigan, 500 Church Street, Ann Arbor, MI 48109, USA; ashking@umich.edu
[2] Institute of Astronomy, University of Cambridge, Madingley Road, Cambridge CB3 0HA, UK
[3] Astronomical Institute 'Anton Pannekoek', University of Amsterdam, Science Park 904, 1098 XH, Amsterdam, The Netherlands
[4] *Chandra* X-ray Science Center, Massachusetts Institute of Technology, NE80-6077, 77 Massachusetts Ave., Cambridge, MA 02139, USA
[5] Array Operations Center, National Radio Astronomy Observatory, 1003 Lopezville Road, Socorro, NM 87801, USA
Received 2010 July 28; accepted 2010 December 2; published 2010 February 7

ABSTRACT

We report on the results of a simultaneous monitoring campaign employing eight *Chandra* X-ray (0.5–10 keV) and six Very Large Array/Extended Very Large Array (8.4 GHz) radio observations of NGC 4051 over seven months. Evidence for compact jets is observed in the 8.4 GHz radio band; this builds on mounting evidence that jet production may be prevalent even in radio-quiet Seyferts. Assuming comparatively negligible local diffuse emission in the nucleus, the results also demonstrate an inverse correlation of $L_{\rm radio} \propto L_{\rm X\text{-}ray}^{-0.72\pm0.04}$. If the A configuration is excluded in the case where diffuse emission plays a significant role, the relation is still $L_{\rm radio} \propto L_{\rm X\text{-}ray}^{-0.12\pm0.05}$. Current research linking the mass of supermassive black holes and stellar-mass black holes in the "low/hard" state to X-ray luminosities and radio luminosities suggests a "fundamental plane of accretion onto black holes" that has a positive correlation of $L_{\rm radio} \propto L_{\rm X\text{-}ray}^{0.67\pm0.12}$. Our simultaneous results differ from this relation by more than 11σ (6σ excluding the A configuration), indicating that a separate mode of accretion and ejection may operate in this system. A review of the literature shows that the inverse correlation seen in NGC 4051 is seen in three other black hole systems, all of which accrete at near 10% of their Eddington luminosity, perhaps suggesting a distinct mode of disk–jet coupling at high Eddington fractions. We discuss our results in the context of disks and jets in black holes and accretion across the black hole mass scale.

Key words: accretion, accretion disks – black hole physics – galaxies: active – galaxies: jets – galaxies: Seyfert

Online-only material: color figures

1. INTRODUCTION

With evidence of supermassive black holes (SMBHs) lurking at the center of nearly all galaxies (Richstone et al. 1998), it is pertinent to examine and understand their properties as well as their impacts. Studies have shown a critical relation between SMBHs and their host galaxies in the form of the M–L and M–σ relations. The M–L relation between the mass of the SMBH and the luminosity of the bulge suggests an intrinsic link between the SMBH and the amount of mass in the bulge assuming a particular mass-to-light ratio (e.g., Magorrian et al. 1998; Kormendy & Richstone 1995; Gültekin et al. 2009b). The M–σ relation between SMBH mass and the velocity dispersion of the host galaxy also implies a physical coupling between formation and growth of the black hole and its surroundings (e.g., Ferrarese & Merritt 2000; Gebhardt et al. 2000). The driving mechanism behind these couplings and the M–σ relation especially is thought to be the result of mergers that drive accretion onto the SMBH, which can quench star formation as energy released from the central engine drives the gas out (Di Matteo et al. 2005).

In particular, the study of an accretion disk around an SMBH begins with observations of the extended blackbody spectrum emitted by the disk; a consequence of the radial dependence of the temperature associated with the accretion disk. In SMBH accretion disks, this spectrum is thought to peak in the UV and is associated with the "Big Blue Bump" (Elvis et al. 1994). Unfortunately, UV flux is extremely susceptible to scattering by dust, and modeling to correct for this can induce large uncertainties. In X-rays, emission from inverse-Compton scattering, magnetic flares, and magnetic reconnection events associated with the accretion disk are characterized well by a non-thermal power law (e.g., McHardy et al. 2004). Accordingly, X-ray flux can be another proxy for observing accretion disks.

In accreting systems, as material migrates toward the center, a fraction is also ejected into outflows that have both radiative and mechanical influences on their environments. The exact physical nature has not yet been observationally determined, but outflows are seen in all types of accreting systems, i.e., protostellar objects (e.g., Mundt 1985), neutron stars and stellar-mass black holes (e.g., Margon 1982), and SMBHs (e.g., Cohen et al. 1979). These outflows can reach supersonic speeds when collimated into jets, eventually depositing significant energy into their surroundings (e.g., Cohen et al. 1979; Fabian et al. 2002; Allen et al. 2006). Material moving outward into their host galaxies also begins to cool via synchrotron radiation (e.g., Jones et al. 1974). Observed in the radio frequencies, this non-thermal process emitted in the core of the system is predicted to have a flat spectrum, independent of frequency (Blandford & Konigl 1979) making it a great observational tool for characterizing jet emission.

Utilizing these two wavelength regimes, Merloni et al. (2003), Falcke et al. (2004), and Gültekin et al. (2009a) have all suggested a "fundamental plane" of black hole activity connecting black hole mass, X-ray luminosity, and radio luminosity. The plane spans over 9 orders of magnitude in mass, 12 orders of magnitude in radio luminosity, and 13 orders of magnitude in

Table 1
X-ray Observations Made by *Chandra* in the Continuous Clocking Mode

Date of Observation (MJD)	Exposure Time (ks)	Count Rate (counts s^{-1})	Γ	Γ Flux (2–10 keV) (10^{-11} erg s^{-1} cm^{-2})	Disk Blackbody Temperature (keV)	Disk Blackbody Flux (2–10 keV) (10^{-15} erg s^{-1} cm^{-2})	χ^2/ν
54838.2	10.2	15.6 ± 0.04	$2.24^{+0.03}_{-0.03}$	$3.27^{+0.09}_{-0.09}$	$0.18^{+0.02}_{-0.02}$	$10.7^{+6.3}_{-3.7}$	646.1/426
* 54874.9	1.1	16.3 ± 0.12	$2.39^{+0.11}_{-0.09}$	$2.58^{+0.17}_{-0.20}$	$0.17^{+0.04}_{-0.03}$	$6.1^{+11.8}_{-4.1}$	244.6/213
54898.3	10.1	5.3 ± 0.02	$1.73^{+0.08}_{-0.03}$	$1.59^{+0.10}_{-0.05}$	$0.17^{+0.01}_{-0.02}$	$4.3^{+2.7}_{-1.0}$	394.0/381
* 54943.1	10.1	4.7 ± 0.02	$2.10^{+0.05}_{-0.07}$	$1.14^{+0.05}_{-0.08}$	$0.18^{+0.03}_{-0.03}$	$3.7^{+4.4}_{-1.4}$	368.0/353
54988.0	10.1	4.6 ± 0.02	$1.33^{+0.06}_{-0.07}$	$1.67^{+0.09}_{-0.12}$	$0.19^{+0.01}_{-0.01}$	$16.0^{+2.1}_{-3.1}$	370.0/394
55005.8	10.1	5.6 ± 0.02	$2.01^{+0.06}_{-0.07}$	$1.23^{+0.07}_{-0.08}$	$0.18^{+0.01}_{-0.01}$	$8.1^{+3.2}_{-2.4}$	501.8/364
55025.4	10.1	13.1 ± 0.04	$2.29^{+0.03}_{-0.03}$	$2.57^{+0.06}_{-0.07}$	$0.18^{+0.02}_{-0.02}$	$5.1^{+4.1}_{-2.2}$	578.7/411
55043.1	10.1	14.9 ± 0.04	$2.29^{+0.03}_{-0.02}$	$2.97^{+0.07}_{-0.06}$	$0.17^{+0.02}_{-0.02}$	$3.5^{+2.3}_{-1.5}$	627.7/420

Notes. The data were modeled using `Xspec`, and unabsorbed fluxes for both the power-law and disk blackbody are presented here. The power law used in the analysis varies by a factor of three. The "*" refers to the observations that were not used in this analysis because of the lack of simultaneous radio measurements.

X-ray luminosity (Merloni et al. 2003). This plane suggests that accretion (traced by X-ray luminosity) and jet production (traced by radio luminosity) are fundamentally linked together. Although the exact coupling is not understood, this relation implies that accretion must be driving jet production.

A known problem with the relation is the large scatter of the data about the plane ($\sigma_{\rm radio} = 0.88$ dex; Gültekin et al. 2009a). This scatter can be attributed to observational errors or the result of non-simultaneity between the observations themselves. Measuring the X-ray and radio luminosities at different times may have sampled different fluctuations in the accretion rate in individual sources, driving them away from the relation. The time between X-ray and radio observations of Merloni et al. (2003) and Gültekin et al. (2009a) is known to span a few years to a decade.

To address these issues, and in order to examine disk–jet coupling at high mass accretion rates, we undertook a simultaneous X-ray and radio monitoring campaign of the Seyfert-1 active galactic nucleus (AGN) NGC 4051. This galaxy is relatively nearby ($z = 0.002336$), and the central black hole mass has been determined through reverberation mapping techniques ($(1.91 \pm 0.78) \times 10^6\,M_\odot$, Peterson et al. 2004; $(1.73 \pm 0.55) \times 10^6\,M_\odot$, Denney et al. 2009). NGC 4051 is typically observed to accrete at approximately 5% of its Eddington luminosity (Peterson et al. 2004). The innermost orbital timescale of NGC 4051 is on the order of a few minutes to hours, defined as $t_{\rm dyn} \sim R/v_\phi$, where R is the radius assumed to be only a few gravitational radii from the black hole and v_ϕ is the orbital velocity. While the viscous timescales are on the order of days to weeks for typical parameters, defined as $t_{\rm vis} \sim t_{\rm dyn}\alpha^{-1}(H/R)^{-2}$, where α is the viscosity parameter in the standard α-disk prescription (Shakura & Sunyaev 1973), and H is the scale height of the disk. Variations in the accretion rate of NGC 4051 are thought to occur on these viscous timescales of a day to weeks. This is further supported by its highly variable spectrum, which is most notable in X-rays that vary up to a factor of 10 on weekly timescales (Uttley et al. 1999). The variability seen in NGC 4051 was essential for our simultaneous monitoring campaign to probe different accretion rates.

In this paper, we present the simultaneous X-ray and radio observations of NGC 4051, in an effort to shed light on the implications of the fundamental plane of accretion onto black holes, and to explore jet production in this Seyfert galaxy.

2. DATA REDUCTION AND ANALYSIS

2.1. X-ray

The Advanced CCD Image Spectrometer (ACIS) on the *Chandra* X-ray telescope was used to collect eight observations of NGC 4051 between 2009 January 1 (MJD 54848.2) and 2009 July 31 (MJD 55043.1). We list these observations of approximately 10 ks exposures in Table 1. X-ray observations are subject to photon pile-up. Photon pile-up is when multiple low-energy photons arrive at the same CCD pixel in a single frame and register identically to one higher energy photon. It reduces the number of soft, i.e., low energy photons that are detected while increasing the hard, i.e., high energy photon counts which can mislead analysis by making the spectrum appear harder than it actually is. To avoid photon pile-up, we used the mode with the minimal integration time, i.e., the continuous clocking mode, with integration times of only 2.85 ms. Such a fast integration time helps to prevent against multiple photons being counted as one higher energy photon, but does so at the expense of one spatial dimension. The resulting image is 1×1024 pixels with a resolution $<1''$, and an effective field of view of $8'.3 \times 8'.3$, with spatial resolution in only one dimension.

We used `HEASOFT` version 6.7, `FTOOLS` version 6.7, `XSPEC` version 12.5.1, `CALDB` version 4.1, and `CIAO` version 4.1 in the data reduction and analysis of these images. The `CIAO psextract` routine was used to extract a spectrum and background for a point source as well as the companion auxiliary response functions and response matrix functions. To do so, we used a circular extraction region of diameter $2''$ centered at $12^{\rm h}03^{\rm m}09^{\rm s}.6$, $+44^\circ31'52''.5$, while another $2''$ diameter circular extraction region was used approximately $20''$ off-source for the background. This aperture size ensured encapsulation of the source, assuming it was a point source and not elongated, but not so large as to include effects from the background.

We analyzed X-ray data between the energy range of 0.5 and 10.0 keV with a minimum of 10 counts per bin. A power-law component modeling the continuum was initially fit to the data. To check for pile-up in our source before further modeling was attempted, we also used an annulus with inner radius of $0''.9$ and outer radius of $1''.7$ to obtain an additional spectrum from each observation using `psextract`. Again, requiring a minimum of 10 counts per bin, we fit power-law models to

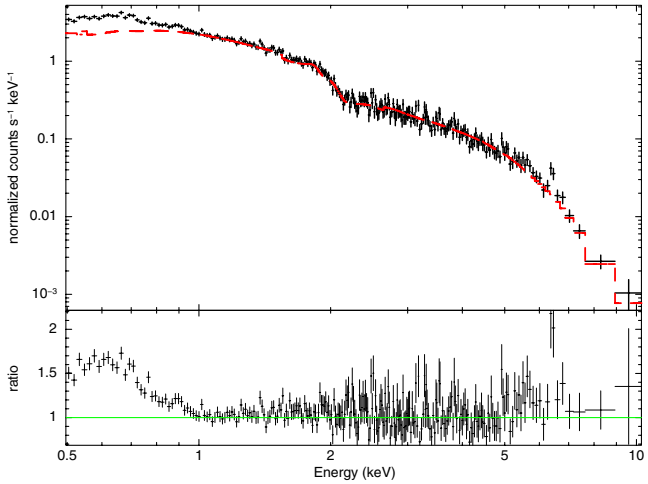

Figure 1. Sample spectrum from MJD 54943.1 modeled with just a power-law component, in red, as the `Xspec` model `phabs(po)*zedge*zedge`. The Galactic absorption was modeled as an effective H column density of 1.15×10^{20} cm^{-2} (Kalberla et al. 2005) and the K-shell absorption edges of O VII and O VIII were frozen at their respective rest energies of 0.739 keV and 0.871 keV. We initially fit the spectrum from 2 to 10 keV and then extended the model to lower energies. The fit produced a $\chi^2/\nu = 1770/366$.

(A color version of this figure is available in the online journal.)

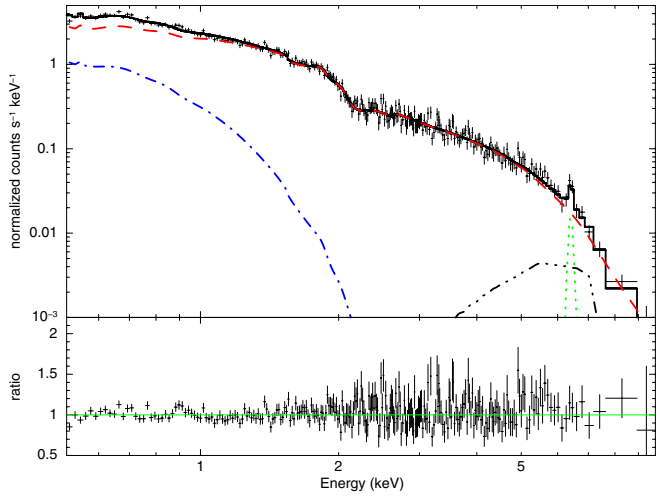

Figure 2. Same spectrum as Figure 1 but now includes a power law, disk blackbody, a narrow Fe Kα line, and a broad Fe Kα line, modeled with `Xspec` model `phabs(po+diskbb+zgauss+laor)*zedge*zedge`. We used the same Galactic absorption and absorption edges as in Figure 1. The power law is the red dashed line. The disk blackbody is the blue dot-dashed line. The narrow Fe Kα line is the green dotted line. The broad Fe Kα line is the black triple-dotted-dashed line. Finally, the solid black line is the sum of all the components. The fit produced a $\chi^2/\nu = 368.0/353$.

(A color version of this figure is available in the online journal.)

the annular spectra for comparison. If pile-up was present, the spectra from the annuli would be softer than those extracted from the central region. In general, we found that the two spectra were equivalent, within errors, suggesting that any pile-up is minimal in all observations.

A description of the line-of-sight absorption is as follows and was included in all modeling. The Galactic absorption was modeled as an effective H column density of 1.15×10^{20} cm^{-2} (Kalberla et al. 2005) using `phabs`. Two absorption edges typical to Seyfert AGN (Reynolds 1997) at K-shell rest energies of O VII and O VIII of 0.739 and 0.871 keV, respectively, were modeled using `zedge`. These three rest-frame values were frozen, while individual normalizations were allowed to vary.

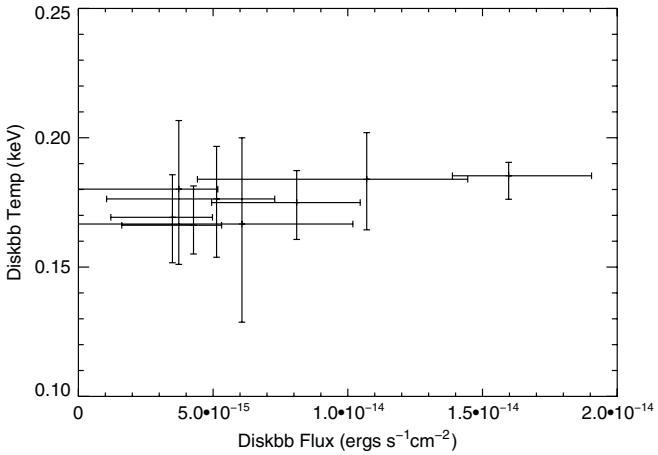

Figure 3. Comparison between the soft-excess disk blackbody temperature and its blackbody flux. A constant temperature independent of flux as seen here suggests a purely phenomenological interpretation of the disk blackbody component.

Figure 1 shows a sample spectrum fit with a simple power-law model. This attempt at fitting the data resulted in a poor fit for all spectra and in particular the spectrum presented in Figure 1 had a χ^2/ν of 1770/366. By looking at the ratio of the data to the model, one can see the obvious excess at low energies typical of Seyfert galaxies (Reynolds 1997). To better characterize the source flux, a disk blackbody component was added shown in Figure 2. Typically, it is thought that this soft excess is not the result of a thermal blackbody component, but of an atomic process that is not trivial to model (e.g., Gierlinski & Done 2004; Crummy et al. 2006). Figure 3 plots the temperature and flux from the putative disk component. We find that the temperature does not vary with flux, suggesting that it is not a blackbody thermal component. However, the addition of the disk blackbody does produce a formally better fit.

In Figure 2, we not only include a power-law component and a disk blackbody, but also an unresolved Gaussian that models a narrow Fe Kα line and a broad Fe Kα line. The fit is improved to $\chi^2/\nu = 368.3/353$. It should be noted that the Fe Kα lines are not detected at more than the 2σ level of confidence, except in the last two exposures. However, they were included in the modeling for completeness (see Table 2). In Seyferts and AGN, Fe K-shell emission due to fluorescence and recombination is the most prominent of the X-ray emission lines (e.g., Miller 2007). The shape and broadening of the Fe Kα line, initially modeled by Fabian et al. (1989) for a zero-spin Schwarzschild black hole and by Laor (1991) for a maximally spinning black hole, are dependent on the spin of the black hole, the inner and outer radii of the emitting region, the inclination angle of the disk and the efficiency of the disk emissivity. With this in mind, we modeled the broad Fe Kα line with the `XSPEC` model `laor` that produces an emission line from an accretion disk and includes general relativistic effects (Laor 1991). Keeping the emissivity as a function of radius ($\propto R^{-3}$), the outer radius fixed at 400 $GM\,c^{-2}$, and the inclination fixed at 30°, we let the inner radius vary.

Finally, in order to compare to the fundamental plane of accretion onto black holes as described by Gültekin et al. (2009a), just the power-law component within the energy range of 2–10 keV was used to compute the total flux associated with each observation. This component contributes to more than 95% of the total flux in the 2–10 keV range, with the broad Fe Kα line

Table 2
X-ray Fe Kα Line

	Narrow			Broad			
Date of Observation (MJD)	Fe Kα (keV)	Equivalent Width (keV)	Flux (10^{-13} erg s^{-1} cm^{-2})	Broad Fe Kα Line (keV)	Rin (GM c^{-2})	Equivalent Width (keV)	Flux (10^{-13} erg s^{-1} cm^{-2})
54838.2	$6.40^{+0.04}_{-NA}$	$0.04^{+0.04}_{-0.04}$	$1.36^{+1.29}_{-1.26}$	$6.95^{+NA}_{-0.61}$	8.2^{+73}_{-5}	$0.31^{+0.24}_{-0.18}$	$7.07^{+5.48}_{-4.11}$
* 54874.9	...	...	...	$6.34^{+0.42}_{-NA}$	5.6^{+20}_{-NA}	$0.54^{+0.80}_{-0.49}$	$10.1^{+15.0}_{-9.18}$
54898.3	$6.45^{+0.09}_{-0.07}$	$0.04^{+0.07}_{-NA}$	$0.84^{+1.31}_{-NA}$	$6.62^{+NA}_{-0.32}$	25^{+165}_{-NA}	$0.15^{+0.38}_{-NA}$	$2.27^{+5.76}_{-NA}$
* 54943.1	$6.40^{+0.05}_{-0.04}$	$0.14^{+0.07}_{-0.07}$	$1.81^{+0.96}_{-0.98}$	$6.91^{+NA}_{-0.56}$	3.1^{+13}_{-NA}	$0.70^{+0.43}_{-0.45}$	$5.67^{+3.53}_{-3.66}$
54988.0	$6.39^{+0.05}_{-NA}$	$0.06^{+0.05}_{-0.05}$	$1.32^{+1.20}_{-1.25}$	$6.35^{+0.13}_{-NA}$	1.2^{+69}_{-NA}	$0.39^{+0.26}_{-0.28}$	$6.59^{+4.52}_{-4.75}$
55005.8	$6.36^{+0.03}_{-NA}$	$0.12^{+0.07}_{-0.10}$	$1.73^{+1.05}_{-1.44}$	$6.34^{+0.61}_{-NA}$	3.3^{+31}_{-NA}	$0.32^{+0.26}_{-0.27}$	$3.94^{+3.20}_{-3.23}$
55025.4	$6.40^{+0.11}_{-NA}$	$0.03^{+0.04}_{-NA}$	$1.02^{+1.31}_{-NA}$	$6.43^{+0.13}_{-NA}$	44^{+20}_{-32}	$0.30^{+0.12}_{-0.11}$	$6.60^{+2.72}_{-2.49}$
55043.1	$6.67^{+0.07}_{-0.08}$	$0.02^{+0.05}_{-0.01}$	$0.64^{+1.45}_{-0.15}$	$6.34^{+0.15}_{-NA}$	20^{+25}_{-9}	$0.29^{+0.12}_{-0.12}$	$7.29^{+2.98}_{-2.86}$

Notes. This table shows the two Fe Kα lines included in the X-ray models. To calculate the narrow Fe Kα lines, `zgauss` with energy restricted between 6.35 and 6.97, a width of $\sigma = 0$ (unresolved), redshift of $z = 0.002336$, and varying normalization was used. For the broad Fe Kα line, `laor`, the energy was restricted to vary from 6.34 to 6.95 keV, the power-law dependence was frozen at 3, the inner edge was allowed to vary from 1.235 to 400 GM c^{-2}, the outer radius was frozen at 400 GM c^{-2}, the inclination angle was frozen at 30°, and the normalization was allowed to vary. All the lines were at least marginally detected and therefore included in modeling techniques, except the narrow Fe Kα on MJD 54874.9, where it registered zero flux for the best fit parameters. The "*" refers to the observations that were not used in this analysis because of the lack of simultaneous radio measurements.

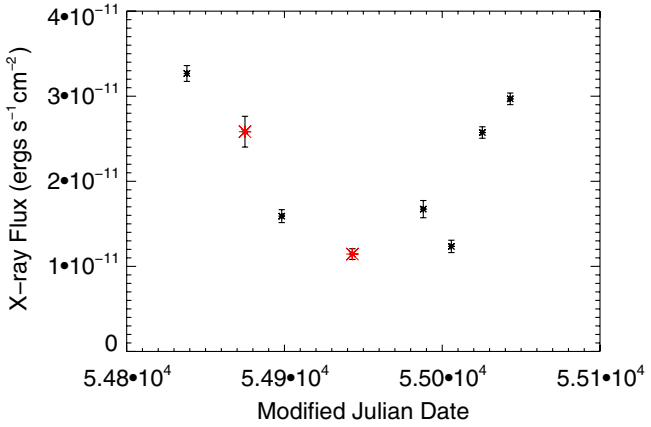

Figure 4. X-ray light curve taken by *Chandra* in the continuous clocking mode between 2 and 10 keV. It shows a variability of a factor of three. The points in red do not have simultaneous radio observations and are not used in the correlation analysis.

(A color version of this figure is available in the online journal.)

contributing 2%–5% of the total flux. We plot this light curve in Figure 4, and list the results for each spectrum in Table 1. The continuum flux varies by almost a factor of three, which can be attributed to fluctuations in the mass accretion rate.

2.2. Radio

A combination of the Very Large Array (VLA) and Extended Very Large Array (EVLA) antennas was used to observe NGC 4051 six times between 2008 December 31 (MJD 54831.3) and 2009 July 31 (MJD 55043.1). These observations were approximately 1 hr integrations centered at 8.4 GHz with a bandwidth of 50 MHz in two channels with two polarizations. We chose this frequency to ensure that the self-absorption of the synchrotron emission was not a problem. Exposure dates and times are listed in Table 3. During each observation, the antennas switched from on source, located at $1^h203^m1^s$ +44°31′8″, to a phase calibrator located at $12^h21^m4^s$ +44°11′4″ every 3.33 s. 3C 286 was used as the flux calibrator with 3.33 s of integration at the end of each observation. During the seven months spanning the observations, the VLA/EVLA evolved from its A configuration, which has its longest baseline of 36.4 km, to its C configuration with a maximum baseline of only 3.4 km. This significantly changed the resolution of the resulting images, and steps were taken to ensure a consistent comparison among the six observations. The resolution during each configuration is listed in Table 3.

The Common Astronomy Software Applications (`CASA`) package, version 3.0.0, developed by the National Radio Astronomy Observatory (NRAO), was used to reduce the radio observations. The routine `setjy` was used to set 3C 286 as the flux calibrator, while the routine `gaincal` set the gain calibration incorporating both the phase calibrator source located at $12^h21^m4^s$ +44°1′4″ and 3C 286 as references. Either antenna VA06, VA08, VA10, or VA12 was used as the reference antenna for these calibrations. Antennas that were off or showed discontinuities that were not characteristic of the overall data in either phase or amplitude were excluded, resulting in only one or two EVLA antennas per data set. The `CLEAN` algorithm was then run to create an image, using a threshold of 0.1 mJy as well as Briggs weighting and robust parameter of 0.5. Briggs weighting provides a smooth transition between natural and uniform visibility weighting and is characterized by a robust parameter where 2.0 is approximately natural weighting and −2.0 is approximately uniform (Briggs 1995). No self-calibration was done because the source was too faint, which is consistent with methods described by Giroletti & Panessa (2009), who also observed NGC 4051 at 8.4 GHz. Figure 5 shows an example of the type of images that were produced.

After the `CLEAN` algorithm was run, the flux density was measured using `CASA`'s `imfit`, which fit Gaussian curves to the peak intensities. Because of the four different configurations, we were only able to resolve structures in the A configuration, as seen in Figure 5, which afforded the best resolution. In order to make a fair comparison between all the measurements, the Gaussian fits were restricted to an area of approximately $8'' \times 6''$, ensuring the inclusion of all the structures present in the images. Fortunately, as seen in the work done by Giroletti & Panessa (2009), there does not appear to be any extensive large-scale diffuse emission that would be resolved out in higher resolution

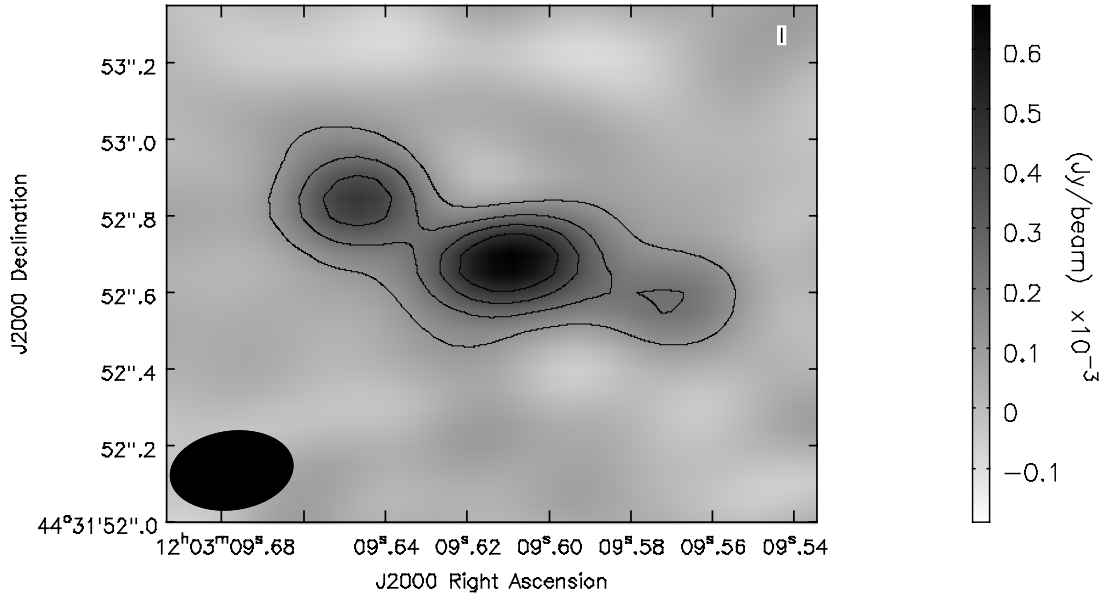

Figure 5. Radio observation made by VLA/EVLA in the A-configuration on 2009 December 31 (MJD 54831.3). The contours are [0.2, 0.4, 0.6, 0.8] × 0.6 mJy beam^{-1}. The beam pattern (3″ × 2″) is also shown in the lower left corner. The center is associated with the black hole, while the extended lobes to the northwest and southeast are associated with the endpoints of jets of the system.

Table 3
Radio Observations

Date of Observation	Exposure Time	Configuration	Resolution		Flux Density	Peak Flux Density
(MJD)	(ks)		(arcsec)	(pc)	(mJy)	(mJy)
54831.3	3.6	A	0.3 × 0.2	15 × 10	1.73 ± 0.06	0.65 ± 0.02
54899.2	3.5	B	0.9 × 0.7	44 × 34	5.99 ± 0.20	1.13 ± 0.04
54987.1	3.6	BnC	2.2 × 0.9	110 × 44	5.66 ± 0.20	1.47 ± 0.05
55005.2	3.6	C	3.1 × 2.3	150 × 110	4.97 ± 0.17	2.22 ± 0.08
55027.0	2.4	C	2.5 × 2.0	120 × 97	4.99 ± 0.20	2.08 ± 0.08
55043.1	3.6	C	3.1 × 2.2	150 × 110	4.78 ± 0.16	2.22 ± 0.08

Notes. This table gives the radio observations taken at 8.4 GHz with a 50 MHz bandwidth in two channels. The VLA/EVLA was in four different configurations during the entire campaign, starting in the A with the longest baseline and ending at C with the shortest baseline. In the analysis, we scaled the observations to 5 GHz as Ho (2002) did.

configurations. If this were the case, the flux would decrease with higher resolution, when in fact Table 3 demonstrates that the flux in the B configuration, a higher resolution, is higher than in the flux in the C configuration, a lower resolution. This strongly suggests that the radio variability observed between the B and C configurations is intrinsic, not instrumental. However, it is unclear if the diffuse emission has been resolved out in the A configuration. For this reason, we quote our results with and without the A array measurements. The measurements are listed in Table 3 and the light curve is shown in Figure 6. The errors in these measurements also include a systematic error of 3% of the total flux, added in quadrature, to account for the calibration errors. These measurements, including the integral flux densities as well as the peak flux densities, do vary by a factor of three, which is comparable to the X-ray variations. In order to compare to Gültekin et al. (2009a), we scaled the fluxes as $F_\nu \propto \nu^{-0.5}$ from 8.4 GHz to 5 GHz as Ho (2002) did.

Inspection of the image produced in the A configuration reveals evidence of jet production. As shown in Figure 5, three structures are present: a central source and two extended lobes. The central radio lobe is likely associated with the black hole, while the northwest and southeast lobes may be associated with the endpoints of the outflows in this system. The alignment and varying brightness between the three lobes suggest that this is a jet structure where the jet is partially projected into our line of sight, placing the northwest lobe closer and less obscured than the southeast lobe. We also note that these lobes are not seen in the point-spread function of the antennas and are therefore not artifacts of the `clean` algorithm. Observations by Christopoulou et al. (1997), Giroletti & Panessa (2009), and Kukula et al. (1995) note similar structures as well as the potential evidence for jet production.

2.3. Comparison

These measurements by themselves can give insights into the physical processes that occur in an AGN, but through a comparison of the X-ray and radio luminosities we can explore how accretion is coupled to jet production. To quantify any correlation between the X-ray and radio fluxes, we calculated Spearman's rank coefficient (ρ). This ρ describes how well a data set exhibits a monotonic behavior between two variables; $\rho < 0$ corresponds to variables that are anti-correlated. We find a ρ of −0.66, with a probability of only 0.16 of zero correlation.

Figure 7 plots the X-ray versus radio luminosities. We assumed a distance of 10.0 Mpc derived from the redshift,

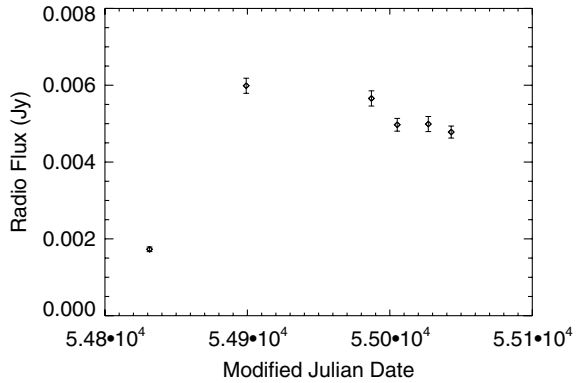

Figure 6. 8.4 GHz light curve taken by the VLA/EVLA. The radio flux density varies by more than a factor of three.

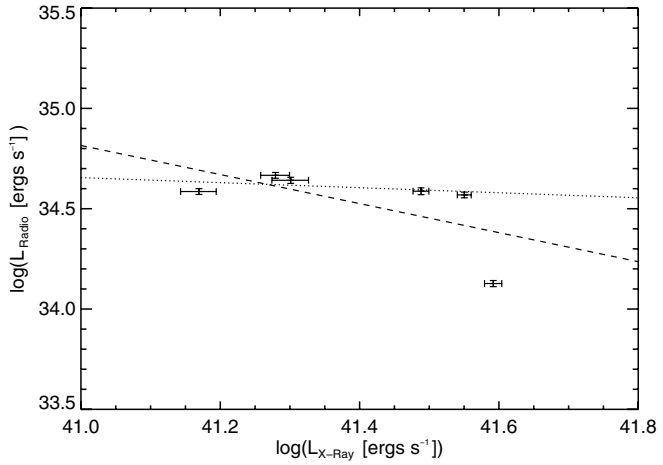

Figure 7. Inverse correlation between the X-ray and radio luminosities. We used the continuum flux from 2 to 10 keV, and we scaled the radio flux as $F_\nu \propto \nu^{-0.5}$ (Ho 2002) from 8.4 GHz to 5 GHz in order to correctly compare to Gültekin et al. (2009a). The dashed line is a fit to our data given by the relation, $\log L_{\rm radio} = (-0.72 \pm 0.04) \log L_{\rm X\text{-}ray} + (64 \pm 2)$. The dotted line excludes the A configuration data point, and is described by the relation $\log L_{\rm radio} = (-0.12 \pm 0.05) \log L_{\rm X\text{-}ray} + (40 \pm 2)$.

$z = 0.002336$ (Peterson et al. 2004), and cosmological parameter $H_\circ = 70$ km s^{-1} Mpc to obtain these luminosities. Figure 7 also includes the least-squares fit of a first-order polynomial to the data points, described by the following relation:

$$\log L_{\rm radio} = (-0.72 \pm 0.04) \log L_{\rm X\text{-}ray} + (64 \pm 2). \quad (1)$$

To test the robustness of the anti-correlation, we used an F-test to compare the results of the first-order polynomial given above to fits with a zeroth-order polynomial as well as the fundamental plane relation of $L_{\rm radio} \propto L_{\rm X\text{-}ray}^{0.64}$. At an 81% confidence level, we were able to rule out the flat model. However, at a 96% confidence level, our model excludes the fundamental plane relation. We also looked at the correlation between the data points excluding the A configuration, in the case that this array resolved out a substantial amount of flux. We found that the correlation was still inversely proportional, described as,

$$\log L_{\rm radio} = (-0.12 \pm 0.05) \log L_{\rm X\text{-}ray} + (40 \pm 2). \quad (2)$$

Using the same F-test, our second model may be consistent with being flat, for it only excludes a flat distribution at the 60% confidence level. However, the positive fundamental plane relation is again excluded, this time at a 98% confidence level.

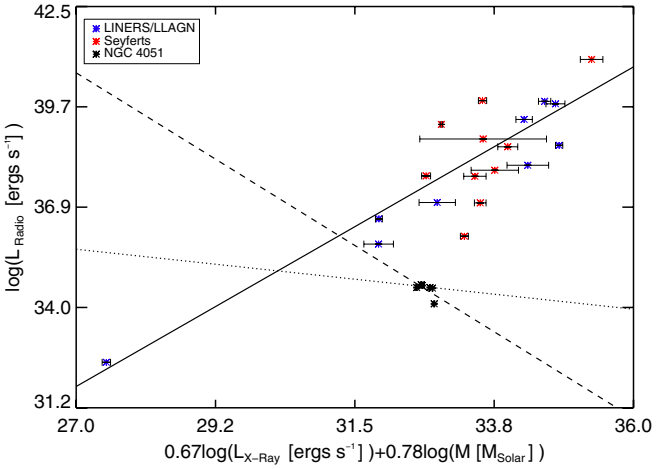

Figure 8. Projection of the fundamental plane of accretion onto black holes as described by Gültekin et al. (2009a). The red points are Seyfert galaxies, while blue points are LINERS or LLAGN. The solid black line is Gültekin et al. (2009a) best-fit line. Our data points are shown in black, with our best fit as the dashed line and dotted lines as described in Figure 7.

(A color version of this figure is available in the online journal.)

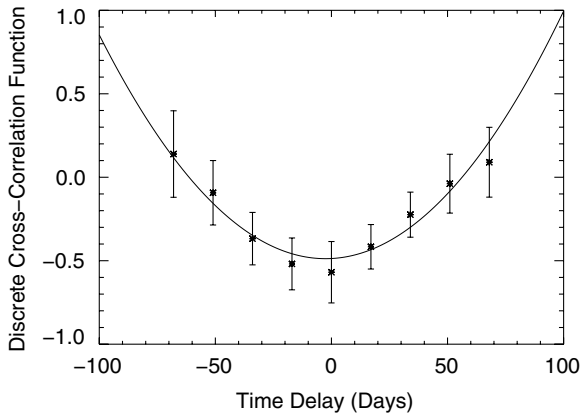

Figure 9. DCCF between X-ray and radio luminosities. We fit the DCCF with a quadratic function, and the minimum occurs at -2.5 ± 5.3 days with a DCCF value of -0.48 ± 0.1. A negative delay implies that the radio is lagging the X-ray.

To place the data from NGC 4051 in context, we plotted our data and best-fit line against the data and the best-fit line described in Gültekin et al. (2009a) in Figure 8. The best-fit line found by Gültekin et al. (2009a) is described as follows:

$$\log L_{\rm radio} = (0.67 \pm 0.12) \log L_{\rm X\text{-}ray} + (0.78 \pm 0.27) \log M_{\rm BH} + (4.80 \pm 0.24). \quad (3)$$

One should notice that our data are not described by the positive correlation of $L_{\rm radio} \propto L_{\rm X\text{-}ray}^{0.67}$ denoted by the solid line, but instead by the dashed line and the dotted line described by $L_{\rm radio} \propto L_{\rm X\text{-}ray}^{-0.72}$ and $L_{\rm radio} \propto L_{\rm X\text{-}ray}^{-0.12 \pm 0.05}$, respectively. In fact, our relation differs from this relation by 11.6σ, while including the A configuration, and 6.5σ, while not including it, when dividing the difference between the power laws by the larger of the two errors. The fundamental plane is known to have a large scatter, and NGC 4051 lies close to the plane. This exercise, however, makes clear how different the X-ray and radio coupling in NGC 4051 appears to be.

Finally, we attempted to quantify whether or not there is a significant time delay between fluctuations in the X-ray and radio

luminosities, which can be seen in Figures 4 and 6, respectively. We used a discrete cross-correlation function (DCCF) as described by Edelson & Krolik (1988) to quantify this delay. The sparse and uneven sampling of the six observations poses a natural limitation on the results of this analysis. This led us to linearly interpolate the data within the seven month period with uniform spacing. The time steps between interpolated points were 17 days, corresponding to the shortest time between observations. White & Peterson (1994) and Gaskell & Peterson (1987) describe similar techniques for interpolating and cross-correlating data in their respective variability studies of AGNs. The results, shown in Figure 9, place the minimum of the DCCF of -0.48 ± 0.1 at -2.5 ± 5.3 days, suggesting that X-ray dips are leading the radio flares.

3. DISCUSSION

In this paper, we present eight *Chandra* X-ray observations and six VLA/EVLA radio observations of Seyfert-1 NGC 4051 taken over a seven month period. By simultaneously measuring in X-ray and radio bands every two to four weeks apart, we are able to probe variations in the accretion rate that occur on the viscous timescale of a few days to weeks in NGC 4051. The observations reveal significant variability in both X-ray and radio bands. The first 8.4 GHz observation on MJD 54831.3 also shows evidence of jet production in the form of two distinct radio lobes, contrary to the idea that radio quiet galaxies like NGC 4051 lack jet production. In fact, the work by Falcke et al. (2001) and that by Nagar et al. (2002) suggest that elongated, non-thermal emission is common in Seyfert and LLAGN. The lobes appear to be resolved into compact impact regions at very high resolution (Giroletti & Panessa 2009). A variability analysis shows that the 2–10 keV X-ray luminosity and 8.4 GHz radio luminosity are inversely correlated according to $L_{\rm radio} \propto L_{\rm X\text{-}ray}^{-0.72\pm0.04}$. This differs by 11.6σ from the current fundamental plane relations which correlates the radio luminosity to X-ray luminosity as $L_{\rm radio} \propto L_{\rm X\text{-}ray}^{0.67\pm0.12}$ for a fixed mass (Gültekin et al. 2009a). Furthermore, if extended emission is resolved out in the highest resolution image, then excluding the A configuration data point, the correlation is $L_{\rm radio} \propto L_{\rm X\text{-}ray}^{-0.12\pm0.05}$. This still differs from the fundamental plane by more than 6σ and is not consistent with the relation.

The results help to shed light on the fundamental plane of accretion onto black holes (Merloni et al. 2003; Falcke et al. 2004; Gültekin et al. 2009a). This plane demonstrates that accretion is linked to jet production, as evidenced by the positive correlation between X-ray and radio luminosity. The measurements in the fundamental plane are generally not simultaneous, and one goal of this study was to understand if simultaneity between X-ray and radio measurements would reduce the scatter in the plane. NGC 4051 was found to lie near the fundamental plane, but showed a negative correlation between X-ray and radio luminosities, contrary to the positive correlation of the plane. The inverse correlation suggests that some systems may lie near the fundamental plane, but vary like NGC 4051, moving across the plane and thus increasing the total scatter.

At least a few other case studies have also shown a separate and inverse correlation deviating from the positive correlation suggested by the fundamental plane. The first is 3C 120, an SMBH with a mass of approximately $5.5 \times 10^7\ M_\odot$ that is observed to accrete at approximately 10% $L_{\rm Edd}$ (Peterson et al. 2004). Chatterjee et al. (2009) present a five year study of 3C 120 using *RXTE* and Very Long Baseline Interferometry to obtain X-ray and radio data, respectively. They use a discrete cross-correlation function to describe the correlation between the X-ray at 2.4–10 keV and the radio at 37 GHz. They find the greatest amplitude in the DCCF to be -0.68 ± 0.11, corresponding to an inverse correlation at a 90% confidence level. This amplitude is consistent with the results of the cross-correlation analysis in NGC 4051. The minimum of the DCCF of 3C 120 cited in Chatterjee et al. (2009) corresponds to a time lag of 120 ± 30 days, with the X-ray dips leading the radio flares. This time delay corresponds to approximately four days in NGC 4051 when scaled using their respective masses, which is consistent with our data.

At the opposite end of the mass scale, the $14\ M_\odot$ black hole GRS 1915+105 (Greiner et al. 2001) sometimes also shows an inverse relation between simultaneous X-ray and radio observations. Rau & Greiner (2003) present a survey of X-ray and radio observations using *RXTE* and the Ryle Telescope between 1996 November and 2000 September. The 1–200 keV X-ray flux showed no correlation to the 15 GHz radio observations. However, the 20–200 keV continuum did show an inverse correlation to the 15 GHz flux described by a Spearman's rank-order correlation coefficient of -0.75. The hard X-ray band in GRS 1915+105 excludes direct emission from the disk, which is consistent with using X-ray emission instead UV emission in NGC 4051 and 3C 120.

The prototypical stellar-mass black hole, Cygnus X-1, may also show an inverse trend at high luminosity. Gallo et al. (2003) study the disk–jet connections in this stellar-mass black hole by analyzing *RXTE* All Sky Monitoring X-ray data from 2–11 keV and the Ryle Telescope radio data at 15 GHz between 1996 January and 2003 January. Cygnus X-1 does follow $L_{\rm Radio} \propto L_{\rm X\text{-}ray}^{0.7}$, until it reaches approximately 2% of its Eddington luminosity when the radio flux density turnovers. Gallo et al. (2003) describe departures from this relation at high X-ray luminosity as quenching of its jet production as Cygnus X-1 moves into its "high/soft" state.

Observations of NGC 4051, 3C 120, GRS 1915+105, and Cygnus X-1 all show that X-ray and radio flux follow an inverse relation when observing at nearly simultaneous times when the sources are emitting at 1%–10% of Eddington. Given that an inverse correlation is seen in a quasar, a Seyfert, and two stellar-mass black holes at high Eddington fractions, it is possible that a distinct mode of the disk–jet coupling holds at high Eddington fractions. This would go beyond a simple quenching of jet production, as discussed by Maccarone et al. (2003) and Gallo et al. (2003), since the jet production does not turn off entirely (evidenced by continuous radio emission and jet structures, especially in NGC 4051 and 3C 120; Giroletti & Panessa 2009; Chatterjee et al. 2009). This is the first study to probe a Seyfert galaxy in X-ray and radio bands on viscous timescales of its inner disk. In the future, we will undertake an extended monitoring campaign of NGC 4051 to further characterize this relation as well as determine any time lags between X-rays and radio fluxes.

The authors acknowledge Joan Wrobel, Phil Uttley, Ian McHardy, and the anonymous referee for their insights and comments that improved this paper. They also acknowledge Steven T. Myers for his help with the CASA software package. J.M.M. acknowledges support through the *Chandra* guest observer program. S.M. acknowledges support from a Netherlands Organization for Scientific Research (NWO) Vidi Fellowship

and from the European Community's Seventh Framework Programme (FP7/2007-2013) under grant agreement number ITN 215212 "Black Hole Universe." E.M.C. acknowledges support provided by NASA through the *Chandra* Fellowship Program.

Note Added in Proof: While our paper was being reviewed, a separate paper on radio and X-ray observations of NGC 4051 was accepted for publication (Jones et al. 2010). Our paper was accepted for publication only days later. Jones et al. (2010) report on many more radio observations, and employed RXTE to obtain X-ray flux points. Treating the possibility of diffuse nuclear emission with great care, Jones et al. (2010) find a nearly flat radio-X-ray correlation. Our results are broadly consistent with that finding when the EVLA observation in the A configuration is excluded. The main advantages of our work are the close timing of radio and X-ray observations, and the ability to separate distinct X-ray flux components in Chandra spectra. Both papers show that NGC 4051 lies significantly below the Fundamental Plane. Within the context of other black holes accreting at high Eddington fractions (a point of emphasis in this paper), both sets of results support the possibility that the coupling between the disk and jet in NGC 4051 may be different than in low-luminosity AGN and other extremely sub-Eddington sources. We thank Ian McHardy and Phil Uttley for helpful conversations regarding NGC 4051 and diffuse nuclear radio flux.

REFERENCES

Allen, S. W., Dunn, R. J. H., Fabian, A. C., Taylor, G. B., & Reynolds, C. S. 2006, MNRAS, 372, 21
Blandford, R. D., & Konigl, A. 1979, ApJ, 232, 34
Briggs, D. S. 1995, BAAS, 27, 1444
Chatterjee, R., et al. 2009, ApJ, 704, 1689
Christopoulou, P. E., Holloway, A. J., Steffen, W., Mundell, C. G., Thean, A. H. C., Goudis, C. D., Meaburn, J., & Pedlar, A. 1997, MNRAS, 284, 385
Cohen, M. H., Pearson, T. J., Readhead, A. C. S., Seielstad, G. A., Simon, R. S., & Walker, R. C. 1979, ApJ, 231, 293
Crummy, J., Fabian, A. C., Gallo, L., & Ross, R. R. 2006, MNRAS, 365, 1067
Denney, K. D., et al. 2009, ApJ, 702, 1353
Di Matteo, T., Springel, V., & Hernquist, L. 2005, Nature, 433, 604
Edelson, R. A., & Krolik, J. H. 1988, ApJ, 333, 646
Elvis, M., et al. 1994, ApJS, 95, 1
Fabian, A. C., Celotti, A., Blundell, K. M., Kassim, N. E., & Perley, R. A. 2002, MNRAS, 331, 369
Fabian, A. C., Rees, M. J., Stella, L., & White, N. E. 1989, MNRAS, 238, 729
Falcke, H., Kording, E., & Markoff, S. 2004, A&A, 414, 895
Falcke, H., Nagar, N. M., Wilson, A. S., Ho, L. C., & Ulvestad, J. S. 2001, in Black Holes in Binaries and Galactic Nuclei, ed. L. Kaper, E. P. J. van den Heuvel, & P. A. Woudt (Berlin: Springer), 218
Ferrarese, L., & Merritt, D. 2000, ApJ, 539, L1
Gallo, E., Fender, R. P., & Pooley, G. G. 2003, MNRAS, 344, 60
Gaskell, C. M., & Peterson, B. M. 1987, ApJS, 65, 1
Gebhardt, K., et al. 2000, ApJ, 539, L13
Gierlinski, M., & Done, C. 2004, MNRAS, 349, L7
Giroletti, M., & Panessa, F. 2009, ApJ, 706, L260
Greiner, J., Cuby, J. G., & McCaughrean, M. J. 2001, Nature, 414, 522
Gültekin, K., Cackett, E. M., Miller, J. M., Di Matteo, T., Markoff, S., & Richstone, D. O. 2009a, ApJ, 706, 404
Gültekin, K., et al. 2009b, ApJ, 698, 198
Ho, L. C. 2002, ApJ, 564, 120
Jones, S., McHardy, I., Moss, D., Seymour, N., Breedt, E., Uttley, P., Kording, E., & Tudose, V. 2010, MNRAS, in press
Jones, T., O'dell, S., & Stein, W. 1974, ApJ, 188, 353
Kalberla, P. M. W., Burton, W. B., Hartmann, D., Arnal, E. M., Bajaja, E., Morras, R., & Pöppel, W. G. L. 2005, A&A, 440, 775
Kormendy, J., & Richstone, D. 1995, ARA&A, 33, 581
Kukula, M. J., Pedlar, A., Baum, S. A., & O'Dea, C. P. 1995, MNRAS, 276, 1262
Laor, A. 1991, ApJ, 376, 90L
Maccarone, T., Gallo, E., & Fender, R. 2003, MNRAS, 345, L19
Magorrian, J., et al. 1998, AJ, 115, 2285
Margon, B. 1982, Science, 215, 247
McHardy, I. M., Papadakis, I. E., Uttley, P., Page, M. J., & Mason, K. O. 2004, MNRAS, 348, 783
Merloni, A., Heinz, S., & Matteo, T. 2003, MNRAS, 345, 1057
Miller, J. M. 2007, ARA&A, 45, 441
Mundt, R. 1985, in Protostars and Planets II, ed. D. C. Black & M. S. Matthews (Tucson, AZ: Univ. of Arizona Press), 414
Nagar, N. M., Falcke, H., Wilson, A. S., & Ho, L. C. 2002, New Astron. Rev., 46, 225
Peterson, B. M., et al. 2004, ApJ, 613, 682
Rau, A., & Greiner, J. 2003, A&A, 397, 711
Reynolds, C. 1997, MNRAS, 286, 513
Richstone, D., et al. 1998, Nature, 395, A14
Shakura, N., & Sunyaev, R. 1973, A&A, 24, 337
Uttley, P., McHardy, I. M., Papadakis, I. E., Guainazzi, M., & Fruscione, A. 1999, MNRAS, 307, L6
White, R. J., & Peterson, B. M. 1994, PASP, 106, 879